Quaternary Geochronology 67 (2022) 101240

Contents lists available at ScienceDirect

Quaternary Geochronology

journal homepage: www.elsevier.com/locate/quageo

Luminescence thermochronometry of feldspar minerals: Optimisation of measurement conditions for the derivation of thermal kinetic parameters using isothermal holding experiments

C. Bouscary *, G.E. King

Institute of Earth Surface Dynamics, Géopolis, University of Lausanne, Switzerland

ARTICLE INFO

Keywords:
Low-temperature thermochronometry
Luminescence
Feldspar
Kinetic parameters
Isothermal holding experiments

ABSTRACT

Luminescence thermochronometry is sensitive to very low temperatures (below ~120 °C), and enables the resolution of thermal histories over sub-Quaternary timescales. Here we apply a multi-elevated-temperature post-infrared infrared-stimulated luminescence (MET-pIR-IRSL) measurement protocol to feldspar minerals to extract thermal histories. These thermal histories depend on the thermal stability of the MET signal, and are based on the thermal kinetic parameters extracted from isothermal decay experiments. However, the derived thermal kinetic parameters vary with experimental conditions, specifically with the isothermal holding temperatures (ITL) used. We analyse samples with independently known thermal histories, together with synthetic thermal history samples and samples with unknown thermal histories to test the validity of thermal kinetic parameters obtained from different combinations of isothermal holding data. This approach is tested on feldspars of different mineralogies and lithologies. We find that the temperatures inferred from inverting the data change, depending both on the number and on the highest ITL temperature used for thermal kinetic parameter derivation. Analysed samples validate the MET-pIR-IRSL protocol for extracting thermal histories, and we suggest that four isothermal holding temperatures between 190 and 250 °C are used for appropriate thermal kinetic parameter derivation.

1. Introduction

Thermochronometry is the quantification of the thermal history of rocks. Different thermochronometric systems have different thermal sensitivities, enabling the reconstruction of different time-temperature histories. Only some thermochronometers are able to constrain low-temperature paths (temperatures below ~120 °C) for reconstruction of the thermal histories of the upper first few kilometres of the Earth's crust (e.g., U-Th/He, ^{4}He/^{3}He, ESR; e.g., Ault et al., 2019). Luminescence thermochronometry (Herman et al., 2010; Li and Li, 2013; Guralnik et al., 2015a; King et al., 2016a; Herman and King, 2018) is a recently developed very-low-temperature thermochronometer with a high sensitivity to temperatures below ~120 °C. It has a very low closure temperature (~30–100 °C, depending on the signal) (Guralnik et al., 2013; King et al., 2016b) that offers the potential to resolve rock cooling, and thus exhumation, over timescales of 10^{3}–10^{6} years, i.e. at sub-Quaternary timescales (Rhodes, 2011; Guralnik et al., 2013, 2015b; King et al., 2016a).

Luminescence thermochronometry is a trapped charge method based on the modelling of electron trapping and detrapping in quartz or feldspar minerals, using kinetic parameters derived from fitting experimental data with numerical models (c.f. Herman et al., 2010; Guralnik et al., 2015a, b). The charges (electrons) trapped in the defects of the lattice of quartz or feldspar minerals can be evicted by either optical or thermal stimulation, or for feldspar minerals, via athermal processes related to quantum mechanical tunnelling, generally referred to as anomalous fading (Wintle, 1977). Constraining these processes of luminescence signal accumulation and loss allows the sample's thermal history to be determined and is usually done for all samples investigated (e.g., Guralnik et al., 2015b; Wu et al., 2015; King et al., 2016a; Biswas et al., 2018). One method through which the thermal kinetic parameters can be constrained is an isothermal holding experiment. Such an experiment comprises irradiating a sample in the laboratory, before holding it at different isothermal temperatures for a range of durations, and measuring the remaining luminescence signal (e.g., Murray and Wintle, 1999; Guralnik et al., 2015a).

* Corresponding author.
E-mail address: chloebouscary@gmail.com (C. Bouscary).

https://doi.org/10.1016/j.quageo.2021.101240
Received 8 June 2021; Received in revised form 5 October 2021; Accepted 9 October 2021
Available online 12 October 2021

Beyond the calibration study of Guralnik et al. (2015b), the validity of the thermal kinetic parameters extracted from isothermal holding experiments for different thermochronometric samples has not been confirmed. Guralnik et al. (2015b) showed that their approach of using three isothermal holding temperatures (ITL) between 190 and 230 °C resulted in thermal kinetic parameters that accurately recovered the temperature for samples from the KTB borehole. However, no study has investigated whether this approach, or the approach of King et al. (2016a) of using seven isothermal holding temperatures between 170 and 350 °C, is appropriate for samples other than the KTB borehole samples. Furthermore no independent validation of the use of multi-signal feldspar protocols for luminescence thermochronometry has been made, despite their use in a number of studies (King et al., 2016a, b; Herman and King, 2018; Lambert, 2018; King et al., 2020). This is at least partly because most geological samples do not have an independently constrained thermal history.

In this contribution, we seek to establish what combination of isothermal temperatures is appropriate for samples of different mineralogies and lithologies by developing an independent method of testing the suitability of multi-signal feldspar methods for luminescence thermochronometry. For this, we use an approach for feldspar extracts (following Li and Li, 2011; King et al., 2016a) that exploits the distinct thermal stabilities of infrared stimulated luminescence (IRSL) signals measured at different stimulation temperatures. This approach has been used previously to derive cooling histories in geological settings (King et al., 2016b; Herman and King, 2018). First, we explore known-thermal history Na-feldspar samples of gneiss and amphibolite from the KTB borehole, before investigating K-feldspar minerals extracted from Nepalese Siwaliks sandstones. We then create calibration samples that mimic the thermal steady-state conditions of the KTB borehole by irradiating samples at high temperatures in the laboratory. We validate the multi-thermochronometric method using these data, before contrasting our results with a set of control samples from different mineralogies (Na-feldspars and K-feldspars) and lithologies (bedrocks, sediments, reference sample, and museum specimens).

2. Luminescence thermochronometry: models and measurements

2.1. Luminescence thermochronometry model and derivation of kinetic parameters

Luminescence thermochronometry exploits the properties of electron traps present in the lattice of quartz and feldspar crystals. A range of different models have been proposed to describe optically stimulated luminescence signal growth and decay (e.g., Li and Li, 2013; Guralnik et al., 2015b; Lambert, 2018). For the purpose of this study, we follow the approach of King et al. (2016a) and describe luminescence signal growth with a single saturating exponential function, signal thermal decay with the band-tail states model (BTS; Poolton et al., 2009; Li and Li, 2013; King et al., 2016a), and athermal decay with the model of Huntley (2006) (Tachiya and Mozumder, 1974). The luminescence signal, or the fraction of occupied electron traps (saturation ratio) $\widetilde{n}$ is thus described by: [1]

$$\frac{d[\widetilde{n}(r',E_b,t)]}{dt} = \frac{\dot{D}}{D_0}\left[1-\widetilde{n}(r',E_b,t)\right] - s\,e^{-\frac{E_t-E_b}{k_b T}}\left[\widetilde{n}(r',E_b,t)\right] - \widetilde{s}\,e^{-\rho'\frac{1}{3}r'}\left[\widetilde{n}(r',E_b,t)\right] \quad [1]$$

where t [s] and T [K] are the time and temperature. The radiation-induced growth (first term on the right-hand side of the equation) of the ratio $\widetilde{n} = \left(\frac{n}{N}\right)$ of n trapped electrons in a total of N electron traps is characterised by $\dot{D}$ [Gy/s], the environmental radiation dose rate, and D_0 [Gy], the fading corrected characteristic dose of saturation. Thermal detrapping (second term) is a function of the Boltzmann constant k_B [eV/K], the thermal frequency factor s [s^{-1}], the activation energy (or trap depth below the conduction band) E_t [eV], and the band-tail state energy level E_b [eV]. Athermal detrapping (third term) is a function of the athermal frequency factor $\widetilde{s} = 3 \times 10^{15}$ s^{-1} (Huntley, 2006), the dimensionless density of the recombination centres ρ' [-], and the dimensionless distance r' [-] between trapped electrons and their recombination centres.

The total accumulation of trapped electrons for a given thermal history is obtained by integrating $\widetilde{n}(r',E_b,t)$ over the range of dimensionless distances, r', and the range of the band-tail states, E_b:

$$\widetilde{n}(t) = \int_{r'=0}^{r'=\infty}\int_{E_b=0}^{E_t} p(r')P(E_b)\widetilde{n}(r',E_b,t)\,dE_b\,dr' \quad [2]$$

where $p(r')$ and $P(E_b)$ are respectively, the probability density distributions of the nearest recombination centres and of the band-tail states.

The kinetic parameters in Eq. (1) that describe the luminescence signal are estimated for each sample through a series of laboratory experiments: the luminescence dose response curve is used to constrain the parameters $\widetilde{n}$ and D_0; measurement of athermal signal loss in a fading measurement is used to constrain the athermal kinetic parameter ρ'; and thermal signal loss is measured using an isothermal holding experiment, that allows constraint of s, E_t, and E_b. The rate of electron trapping, $\dot{D}$, is determined from measuring the concentration of U, Th, and K in the sample using, e.g., inductively coupled plasma mass spectrometry (ICP-MS) or gamma-spectrometry.

2.1.1. Athermal detrapping

Athermal detrapping, also referred to as anomalous fading, is a phenomenon that mainly affects feldspar minerals whereby trapped charges tunnel from the electron traps with time (Wintle, 1973, 1977). This tunnelling process is described by the model of Huntley (2006):

$$\widetilde{n}(t^*) = \widetilde{n}(0)\varphi(t^*) \quad [3]$$

where φ is a time-dependent factor,

$$\varphi(t^*) = e^{-\rho' \ln(1.8\,\widetilde{s}\,t^*)^3} \quad [4]$$

with $\widetilde{n}(0)$ being the initial trapped charge quantity, t^* [s] the fading time, and $\rho' \equiv \frac{4\pi\rho}{3\alpha^3}$, where α [m^{-3}] is a constant (Huntley, 2006; Kars et al., 2008; Li and Li, 2008), and ρ [m^{-3}] is the density of randomly distributed recombination centres within the feldspar minerals.

2.1.2. Electron trapping

The accumulation of the luminescence signal through time is fitted with a single saturating exponential function (Guralnik et al., 2015a; King et al., 2016a).

$$\widetilde{n}(t) = \varphi(t^*)\,A\left(1 - e^{-\frac{\dot{D}\cdot t}{D_0}}\right) \quad [5]$$

where φ is a time-dependent factor to account for athermal detrapping throughout measurement as defined in Section 2.1.1 (Eq. (4)), and A is a

pre-exponential multiplier (King et al., 2016a).

2.1.3. Thermal detrapping

Thermal detrapping can be described with different models (Guralnik et al., 2015a), but here we opt to use the BTS (Li and Li, 2013), as implemented by King et al. (2016a):

$$\frac{\tilde{n}(t)}{\tilde{n}(0)} = \varphi(t^*) \int_{E_b=0}^{E_t} P(E_b) e^{\left(-s.t.e^{\frac{E_t-E_b}{k_b T}}\right)} dE_b \quad [6]$$

The probability of thermally evicting an electron into the band-tail states of energy $E_b + dE_b$, with a probability of $P(E_b)dE_b$, is given by (Poolton et al., 2009; Li and Li, 2013):

$$P(E_b)dE_b = B.e^{\left(-\frac{E_b}{E_u}\right)} dE_b \quad [7]$$

where E_u [eV] is the width of the Urbach tail, and B is a pre-exponential multiplier.

2.2. Sample description

2.2.1. KTB borehole samples

Guralnik et al. (2015b) validated the luminescence thermochronometry method by recovering the temperatures of several Na-feldspar samples from the KTB borehole using a single thermochronometric system (IRSL 50 °C). Guralnik et al. (2015b) used a general order kinetic (GOK) model to derive thermal kinetic parameters from three sets of isothermal holding data measured at 190, 210, and 230 °C. In our study, we pursue a multi-thermochronometer approach (Li and Li, 2012), using the multi-elevated temperature (MET) protocol (IRSL 50, 100, 150, 225 °C) (Li and Li, 2011), and the BTS model (Li and Li, 2013) to fit our isothermal decay data. Following King et al. (2016a), we measure isothermal decay for seven different ITL temperatures between 170 and 350 °C.

To validate the MET luminescence thermochronometry method, previously prepared and studied Na-feldspar samples from the KTB borehole, Germany were used (Guralnik et al., 2015b). The KTB borehole (location: 49.83 °N, 12.12 °E, 513 masl) was drilled in south-west Germany through Variscan crystalline basement to a depth of ~9 km (Hirschmann et al., 1997; Wagner et al., 1997), crossing intensely folded and foliated steeply-dipping units of metabasite and gneiss. The area has been tectonically stable over 10's of millions of years, and the rocks reached thermal steady state around 25 Myr ago (Coyle et al., 1997). Since being drilled, several temperature logs and long-term measurements at different depths document the temperature profile of the KTB borehole, making the KTB samples ideal candidates for calibration samples for thermochronometry (e.g., apatite fission-track: Coyle et al., 1997; ^{40}Ar-^{39}Ar: Warnock et Zeitler, 1998; luminescence IRSL 50 °C: Guralnik et al., 2015b). Following the previous work of Guralnik et al. (2015b), four samples that reflected borehole temperatures (i.e. that were not in luminescence athermal steady-state) were selected: samples KTB.253F, KTB.383C, KTB.428B, and KTB.481B (see Table 1).

2.2.2. Butwal samples

In contrast to the KTB samples which comprise Na-feldspar, K-feldspar is the most frequent mineral used in luminescence thermochronometry studies (e.g. King et al., 2016b; Brown et al., 2017; Biswas et al., 2018). No K-feldspar bearing samples with independent temperature control were readily available for calibration of the luminescence thermochronometry technique. Instead, we used a sample from the Himalayas, for which we developed a synthetic calibration by irradiating the sample at elevated temperature within a modified luminescence reader (e.g., Wallinga et al., 2002).

We selected five samples from the Himalayan foreland, taken along the Tinau river in the Siwalik hills (Table 2, and Supplementary material S1, Table S1): BUT.1, 2, 3, 4, and 5. These five Middle Siwaliks sandstone samples are part of the Butwal transect, and were collected between the Main Frontal Thrust and the Main Boundary Thrust. For a geological description of the area, see Gautam and Apple (1997), and Szulc et al. (2006).

2.2.3. Control samples

To evaluate whether different feldspar minerals and lithologies require different measurement conditions for the derivation of thermal kinetic parameters, data from ten previously analysed feldspar samples from the literature, and two further museum-specimens of Na-feldspar, were investigated as control samples. The samples were separated into different categories based on their orthoclase (Or, $KAlSi_3O_8$), albite (Ab, $NaAlSi_3O_8$), and anorthite (An, $CaAl_2Si_2O_8$) composition (Table 3, and Ternary plot in Fig. S2 of the Supplementary material S2).

Table 2
Butwal sample details. Lithologies from Tokuoka et al. (1988). For full details of the dose-rate calculation see Section 2.3.2 and Supplementary material S3, Tables S3.1 and S3.2.

Samples Butwal			Whole-rock radiochemistry			Dose rate
ID	Alt. [m]	Lithology	U [ppm]	Th [ppm]	K [wt. %]	$\dot{D}$ [Gy/ka]
BUT.5	322	Sandstones, Middle Binai Khola Fm./Middle Siwalik	1.8	5.2	0.75	2.08 ± 0.11
BUT.4	317	Sandstones, Lower Binai Khola Fm./Middle Siwalik	1.8	7.3	1.24	2.59 ± 0.14
BUT.3	298	Sandstones, Upper Arung Khola Fm./Lower Siwalik	1.9	8.3	1.22	2.65 ± 0.14
BUT.2	300	Sandstones, Upper Arung Khola Fm./Lower Siwalik	1.7	7.6	0.95	2.36 ± 0.12
BUT.1	204	Sandstones, Upper Arung Khola Fm./Lower Siwalik	1.7	9.2	0.83	2.37 ± 0.12

Table 1
KTB borehole sample details after Guralnik et al. (2015b).

Samples KTB				Whole-rock radiochemistry			Dose rate
ID	Depth [m]	In-situ temperature [°C]	Lithology	U [ppm]	Th [ppm]	K [wt.%]	$\dot{D}$ [Gy/ka]
253F	1175	39.8 ± 2.1	Garnet-amphibolite	0.8	2.1	1.25	1.58 ± 0.24
383C	1730	55.1 ± 2.9	Sillimanite-muscovite-biotite-gneiss	2.5	7.7	1.72	3.02 ± 0.45
428B	1892	59.5 ± 3.1	Garnet-sillimanite-biotite-gneiss	2.6	8.9	2.42	3.44 ± 0.52
481B	2097	65.2 ± 3.4	Garnet-sillimanite-biotite-gneiss	2.7	8.7	2.34	3.58 ± 0.54

Table 3
Mineralogical composition of feldspars of different origins and lithologies. Ternary plot in the Supplementary material S2 (Fig. S2).

ID	Type	Lithology	Feldspar composition assuming 100 % feldspar			Quartz content
			Or (K)	Ab (Na)	An (Ca)	[%]
NB139[a]	B	Migmatitic gneiss, Namche Barwa, Nepal	**89.3**	9.4	1.4	4.2
NB120[a]	B	Migmatitic gneiss, Namche Barwa, Nepal	**86.2**	11.0	2.9	5.0
MBT-I-2430[a]	B	Calc-alkaline granite, Mont-Blanc Tunnel, Italy	**86.7**	12.0	1.3	4.2
KRG-16-06[a]	B	Kurobegawa granite, Japanese Alps, Japan	**79.4**	17.3	3.2	3.1
KRG-16-112[a]	B	Kurobegawa granite, Japanese Alps, Japan	**75.2**	21.3	3.5	3.4
JSH1-13[a]	S	Sand, Shirasuka Lowlands, Japan	**50.4**	37.6	12.1	38.1
HAM-5[a]	S	Lake sediment, Lake Hamana, Japan	**64.9**	31.1	4.0	19.3
F1[a]	R	IAEA AQCS reference feldspar	**61.3**	33.4	5.4	0.3
CLE[a]	M	Pegmatite, Golonca District, Minas Gerais, Brazil	0.5	**99.3**	0.2	3.9
Al-I[b]	M	Metamorphic albite, Pinzele, Trente, Italy	1.0	**97.0**	2.0	5.0
KNR16962[c]	M	Albite, Ljosland, Iveland, Agder, Norway	4.6	**81.6**	13.8	64.7
KNR32491[c]	M	Albite, Seiland, Alta, Finnmark, Norway	4.3	**71.6**	24.0	61.7
KTB.253F[d]	B	Garnet-amphibolite, KTB borehole, Germany	5.9	**68.8**	25.3	21.9
KTB.383C[d]	B	Sillimanite-muscovite-biotite-gneiss, KTB borehole, Germany	18.2	**67.4**	14.4	52.8
KTB.428B[d]	B	Garnet-sillimanite-biotite-gneiss, KTB borehole, Germany	8.2	**77.9**	13.8	51.5
KTB.481B[d]	B	Garnet-sillimanite-biotite-gneiss, KTB borehole, Germany	15.6	**66.7**	17.8	72.5
BUT.5[e]	S	Sandstones, Middle Binai Khola Fm./ Middle Siwalik, Nepal	**96.0**	2.6	1.4	81.2
BUT.4[e]	S	Sandstones, Lower Binai Khola Fm./ Middle Siwalik, Nepal	**89.0**	11.0	0.0	55.3
BUT.3[e]	S	Sandstones, Upper Arung Khola Fm./ Lower Siwalik, Nepal	**86.3**	13.6	0.1	51.4
BUT.2[e]	S	Sandstones, Upper Arung Khola Fm./ Lower Siwalik, Nepal	**88.4**	11.4	0.2	70.2
BUT.1[e]	S	Sandstones, Upper Arung Khola Fm./ Lower Siwalik, Nepal	**95.8**	0.0	4.2	90.8

Notes: Data taken from:
B: Bedrock; S: Sedimentary rocks; R: Reference sample; M: Museum-specimen.
[a] Riedesel et al. (2019).
[b] Riedesel et al. (2021).
[c] X-Ray Fluorescence (XRF) at the University of Lausanne.
[d] Guralnik et al. (2015b).
[e] Mineralogical composition determined using an XRF-attachment fixed to a Risø OSL/TL reader (Kook et al., 2012) at the Leibniz Institute of Applied Geophysics in Hannover.

2.3. Luminescence measurements

2.3.1. Sample preparation

Feldspar minerals were extracted using standard methods (e.g. King et al., 2016a) under subdued red-light conditions. The outer part of the samples (1–3 cm) was removed using a water-cooled diamond saw to remove any potentially light exposed material. The light safe samples were then crushed and sieved to extract the grain-size fraction of interest (180–210 μm). Carbonates and organic material were removed using 10 % HCl and 30 % H_2O_2 respectively. Finally, the K-feldspar enriched fraction was isolated using density separation with sodium polytungstate of $\rho < 2.58$ g.cm^{-3}. The two Na-feldspar museum-specimens KNR16962 and KNR32491 prepared for this study were directly hand-crushed to sand-sized fragments.

2.3.2. Environmental dose rate Ḋ

For the Butwal samples, the dose rate $\dot{D}$ was calculated for each sample. A representative sub-sample of the light exposed sample exterior was sent to ActLabs – Activation Laboratories Ltd, Ancaster, Canada, for ICP-MS analysis to determine the concentration of U, Th and K for environmental dose rate determination. To be able to correct for grain size attenuation effects, the original grain size of the samples (before crushing) were estimated from thin-section images using the software Digital Grain Size developed by Buscombe (2013). When the average grain size of the sample was equivalent to or smaller than the grain size of the feldspar extract analysed (180–210 μm), the latter grain size was adopted for the dose rate calculations. The dose rate was then determined using the Dose Rate and Age Calculator DRAC developed by Durcan et al. (2015), with the conversion factors of Guérin et al. (2011), the alpha grain-size attenuation factors of Brennan et al. (1991), and the beta grain-size attenuation factors of Guérin et al. (2012). An alpha-efficiency (a-value) of 0.15 ± 0.05 (Balescu and Lamothe, 1994), and a water content of 25 ± 10 % were used for the sandstone samples of the Butwal transect. No cosmic dose rate was incorporated in the final dose rate estimations as the samples are thought to have been at the surface for a relatively short period of time.

The DRAC input and output tables for the Butwal samples are provided in the Supplementary material S3, Table S3.2. For samples for which it was not possible to calculate an environmental dose rate, such as the museum specimens for which only a limited amount of material was available, a dose rate of 3.00 ± 0.50 Gy/ka was arbitrarily assumed (see Supplementary material S4, Table S4).

2.3.3. Luminescence thermochronometry measurement protocol

Samples were measured in the luminescence laboratory at the University of Lausanne, Switzerland. Feldspar grains were mounted on 10 mm diameter stainless steel discs as small aliquots of ~2 mm diameter. Three aliquots were measured for each sample for the luminescence thermochronometry measurements (dose response curve, fading, isothermal decay). The measurements were done on TL/OSL-DA-20 Risø luminescence readers, and signals were detected in the blue part of the visible spectrum using a BG39 and BG3 filter pack.

A multi-elevated temperature (MET) post-infrared infrared-stimulated luminescence (post-IR IRSL) – MET-pIR-IRSL – protocol (Li and Li, 2011) was used for all measurements. All of the measurements were done under the same conditions. After a preheat at 250 °C for 60 s, four IRSL measurements at 50, 100, 150 and 225 °C were made for a duration of 100 s each (L_x). A test dose of 75–95 Gy (beta radiation) was given to the aliquots, before measuring the test dose signal (T_x) for each stimulation temperature (50, 100, 150, and 225 °C). Each measurement cycle

was followed by infrared bleaching at 290 °C for 60 s. All luminescence signals were integrated over the 5 first channels (2 s) of the luminescence decay curve, with a background subtraction calculated over the last 50 channels (20 s). Aliquots were accepted and included in the study when they fulfilled all of the sample acceptance criteria, i.e. signal greater than 3σ above background, recycling ratio within 10 % of unity, maximum test dose uncertainty <10 %, and recuperation <10 % of the natural signal.

To constrain the fraction of trapped charge $\tilde{n}$, the natural luminescence signal stored in the feldspar minerals was first measured with the four stimulation temperatures. Nine regenerative doses between 0 and 6000 Gy were then given to the aliquots to construct sample specific dose response curves. Data were fitted using Eq. (5) to derive D_0.

Athermal signal loss was then measured under the same conditions, using the same aliquots. After the administration of a fixed regenerative dose of 75–95 Gy, equal to the test dose, aliquots were preheated prior to storage following Auclair et al. (2003) and measured following different delay periods. Data were fitted using Eq. (3) and (4) and the model of Huntley (2006) for the natural samples; the approach of Kars et al. (2008) was used to screen whether the samples were in athermal steady-state, or whether they exhibited disequilibrium (i.e. contained a thermal signal), through comparison of $\tilde{n}_{nat}$ values with those predicted for athermal steady-state $\tilde{n}_{SS}$ calculated using equation 15 of Li and Li (2008).

Finally, thermal signal loss was measured using isothermal decay measurements on one representative aliquot of each of the samples. The isothermal decay of each signal was measured using storage temperatures in the range of 170–350 °C, with isothermal delay times of 1–10,000 s. All data were fitted using the band tail states model (Li and Li, 2013), using Eq. (6) and (7) to extract the thermal kinetic parameters E_t, E_u, and s.

To control the quality of the data, a dose recovery test was done on each of the KTB and Butwal samples. Six new aliquots were prepared and bleached with natural sunlight for 4 h; three discs were then given a laboratory dose, whilst the other three discs were used to measure the unbleached residual signal. Dose recovery ratios were calculated following residual subtraction. Two different doses were given to the samples, either a dose similar to the D_e of the IRSL.50 signal was used, or a dose of 150 Gy. This second approach was used more widely as most of the Butwal samples are saturated or close to saturation, prohibiting the use of a dose equal to their D_e.

2.4. Data inversion for isothermal temperature

Guralnik et al. (2015b) successfully constrained the thermal histories of the KTB samples using the GOK model and three isothermal holding temperatures at 190, 210 and 230 °C. In contrast, King et al. (2016a) used seven different temperatures to determine thermal kinetic parameters for samples from Namche Barwa, ranging in temperature from 170 to 350 °C. To evaluate whether there is any benefit in using a larger range of isothermal holding temperatures, which necessarily increases sample measurement time, luminescence signals using different combinations of ITL measurements were compared using forward and inverse modelling.

To evaluate the sensitivity of the thermal kinetic parameters to the inclusion/exclusion of different ITL measurements, ITL data were excluded or included in different combinations of three to seven temperatures. The resulting kinetic parameters were then used together with the $\tilde{n}_{nat}$ values to invert for isothermal temperature using Eq. (1) and (2) and the approach described below. Whilst the KTB samples are assumed to have experienced an isothermal history, this is not necessarily the case for the Butwal samples. However, inverting these data for isothermal temperature enables the effect of different ITL combinations to be tested.

For each set of kinetic parameters determined using a different combination of ITL data, a Monte Carlo model with 100 iterations randomly sampled values of the thermal kinetic parameters (E_t, E_u, and s) from within their 1σ uncertainties. Synthetic modelled trapped-charge concentrations ($\tilde{n}_{mod}$) for each IRSL signal were then generated for different isothermal histories, using Eq. (1) and (2), that describe the growth and loss of the luminescence signal through time. The model assumed isothermal holding over a period of 1 Myr to ensure that the luminescence signals generated were in steady-state (i.e., were in a dynamic equilibrium between rates of electron trapping and detrapping), rather than reflecting continued signal growth. Temperatures ranging from 0 to 100 °C in 1 °C intervals were modelled for the natural temperature of the KTB and Butwal samples. Finally, the data were passed through a rejection algorithm (Tarantola, 2005), as described below. The final $\tilde{n}_{mod}$ value, $\tilde{n}_{mod}(end)$, which reflects the trapped-charge concentration for thermal steady-state given the model set-up, was extracted for each synthetic isothermal history, and contrasted with the $\tilde{n}_{nat}$ values to calculate the misfit, after Wheelock et al. (2015), as previously implemented by King et al. (2020) and Biswas et al. (2020):

$$Misfit = \left(0.5\left(\frac{\tilde{n}_{nat}}{s\tilde{n}_{nat}}.\ log\frac{\tilde{n}_{nat}}{\tilde{n}_{mod}(end)}\right)\right)^2 \quad [8]$$

with $s\tilde{n}_{nat}$ being the uncertainty on $\tilde{n}_{nat}$. From this, the likelihood is calculated:

$$Likelihood = exp\ (-Misfit) \quad [9]$$

When likelihood values are close to 1, it indicates a very low degree of misfit between $\tilde{n}_{mod}(end)$ and $\tilde{n}_{nat}$, whereas when values are close to 0, it indicates a higher deviation from the measured $\tilde{n}_{nat}$ values. Likelihood scores are compared to a random number between 0 and 1. If the likelihood is greater than this number, the isothermal history is accepted, otherwise it is rejected (Tarantola, 2005). In this way, thermal histories from the full range of possibilities can be accepted, but the probability of accepting histories with a bad fit (low likelihood) is low. The retained inverted isothermal temperatures are then transformed into a probability density function (pdf) by dividing the temperature and likelihood axes into 100 intervals each, and then summing the number of accepted isothermal temperature paths that pass through each cell (Fig. 1).

2.5. High temperature irradiation experiments

Natural samples in thermal steady-state that have experienced a known-isothermal history, such as the Na-feldspars of the KTB borehole, are not always readily available. Instead, it may be possible to create artificial calibration samples in the laboratory by irradiating samples at elevated temperatures. Sample BUT.4 (K-feldspar) and sample KTB.428B (Na-feldspar) were chosen as synthetic calibration samples.

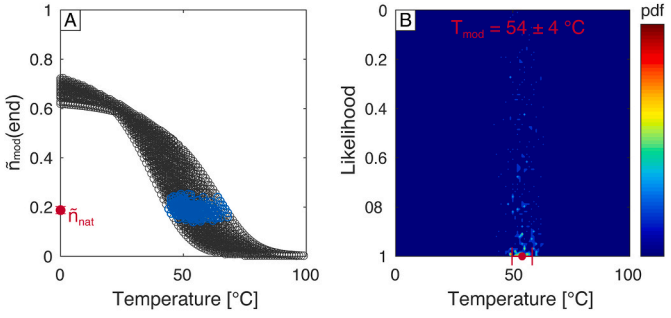

Fig. 1. Inversion of the IRSL.50 signal of sample KTB.383C, using kinetic parameters derived from four isothermal temperatures at 190, 210, 230, and 250 °C. A. Distribution of the $\tilde{n}_{mod}(end)$ values for different isothermal temperature predictions. The red dot represents the $\tilde{n}_{nat}$ value, and the blue area highlights the data that passed the rejection algorithm. B. Probability density function (pdf) resulting from the accepted data in A.

While BUT.4 was selected as a suitable synthetic calibration sample because of its favourable luminescence properties, sample KTB.428B serves to confirm the validity of the synthetic calibration experiment.

Prior to irradiation of the sample at elevated temperature, it is first necessary to predict luminescence trap occupancy for the specific thermal electron trapping and detrapping rates. The natural dose rate of sample BUT.4 is $\dot{D}_{nat} = 2.59 \pm 0.14$ Gy/ka, however at the time of the experiment in the laboratory, the instrument dose rate was $\dot{D}_{lab} \approx (3.627 \pm 0.095) \times 10^9$ Gy/ka $= 0.116 \pm 0.003$ Gy/s, which is nine orders of magnitude greater. In the same manner, the natural dose rate of sample KTB.428B is $\dot{D}_{nat} = 3.44 \pm 0.52$ Gy/ka, and $\dot{D}_{lab} \approx (3.595 \pm 0.095) \times 10^9$ Gy/ka $= 0.114 \pm 0.003$ Gy/s at the time of the experiment. As laboratory dose rates are so much greater than those in nature, it is practical to rapidly irradiate a sample into a thermal steady-state condition, within a matter of hours.

Using Eq. (1) and (2), synthetic $\tilde{n}_{mod}$ values were calculated for a range of different isothermal histories, for each IRSL signal. These forward models were run assuming laboratory irradiation and isothermal holding over a period of 24 h to ensure that thermal steady-state was reached, at temperatures ranging from 0 to 300 °C in 10 °C intervals. Note however that thermal equilibrium is reached after only a few minutes to a few hours of irradiation, dependent on the isothermal temperature and on the luminescence signal measurement temperature. The results of the forward modelling are shown in Table 4. The average uncertainty on the $\tilde{n}_{nat}$ values of the samples investigated here is ~0.03, which is effectively the limit of detection for our measurements. For that reason, three temperatures were selected for sample BUT.4, between which the $\tilde{n}_{mod}$ values differed by > 0.03. Irradiations at 200 °C, 250 °C, 300 °C were selected as they result in measurably different $\tilde{n}$ values (Fig. 2). Irradiation at 250 °C only was carried out for sample KTB.428B as this sample provides validation of the approach.

Experimentally, three aliquots of each sample were first bleached with a solar simulator for 1 h, to remove all pre-existing luminescence signals. They were then placed in a Risø TL-DA-20 instrument (instrument 355), where after irradiation for 24 h at high temperature (200, 250, and 300 °C), dose response curves were measured at ambient laboratory temperatures (~20–25 °C) using the protocol described in Section 2.3.3 to constrain the laboratory induced trapped charge concentration $\tilde{n}_{synth.lab}$. The samples were then inverted for irradiation temperature using the existing isothermal decay and anomalous fading data, and the modelling approach described in Section 2.1. To evaluate which temperature these high temperature irradiation experiments would correspond to under natural environmental irradiation conditions, the data were again inverted, replacing the laboratory dose rate by the natural sample dose rate.

3. Results

3.1. Luminescence measurements

All of the samples were measured following the protocol described in Section 2.3. The four KTB borehole (Germany) samples, and the five Butwal transect (Nepal) samples passed the aliquot acceptance criteria for all IRSL measurements, and the measurements were reproducible within error for each sample ($n = 3$). The IRSL.50 signals were generally brighter than the other IRSL signals. This was particularly evident for the KTB samples, for which post-IR signals were ~75 % less bright, but still yielded good counting statistics.

For the isothermal holding data (Fig. 3C and 3F), the BTS model fits the data well for the lower holding temperatures (170–200 °C). However, there is a misfit in the lower part of the curves between the measured and modelled values for the 250, 300, and 350 °C ITL temperatures. Such a misfit between measured and modelled isothermal decay data has been reported previously for isothermal decay data measured for K-feldspar samples from the Mont-Blanc massif (Lambert, 2018) and Namche Barwa (King et al., 2016a).

The KTB and Butwal samples investigated here exhibit different behaviours regarding their thermal and athermal stabilities (Fig. 3G and 3H). $\tilde{n}_{nat}$ values are thermally and athermally dependent, whereas the $\tilde{n}_{SS}$ values are computed considering only athermal loss. Whereas the KTB samples exhibit similar $\tilde{n}_{nat}$ and $\tilde{n}_{SS}$ values between the three post-IR temperatures at 100, 150, and 225 °C (Fig. 3G), results of the four IRSL measurement temperatures for the Butwal samples are distinct (Fig. 3H), as has been observed previously $\tilde{n}_{nat}$ values are computed considering only athermal signal loss. for MET signals for K-feldspar samples from Namche Barwa (King et al., 2016a). For the KTB samples, the IRSL.50 $\tilde{n}_{nat}$ values are lower than the values of the other IRSL temperatures, explained by lower thermal and athermal stability. This is revealed by the E_t values and fading rates reported in Table 5. The similarity between the $\tilde{n}_{nat}$ values of the post-IR signals of the KTB samples indicates that they have similar stabilities (Table 5), and seems to be a property of these samples, rather than relating to Na-feldspars generally. The other Na-feldspars investigated in this research yield increasing $\tilde{n}_{nat}$ values with increasing temperature (Supplementary materials S5, Fig. S5). In contrast, the Butwal samples show an increase in $\tilde{n}_{nat}$ values with an increase in IRSL measurement temperature. These samples are closer to saturation than the KTB samples, but almost all $\tilde{n}_{nat}$ values are below 86 % of $\tilde{n}_{SS}$, which is the saturation limit ($2D_0$). An exception is the IRSL.150 signal of sample BUT.1 that is fully saturated ($\tilde{n}_{nat} > \tilde{n}_{SS}$), and the IRSL.225 signal of sample BUT.5 that is just at the upper limit of saturation (Fig. 3H).

The thermal kinetic parameters are similar between samples from the same study site, and do not exhibit any systematic trend with increasing stimulation temperature (Table 5). This is in contrast to the results of King et al. (2016a) who found that E_t increased with stimulation temperature for samples from the Namche Barwa; however, the uncertainty on the E_t values reported in this study is greater than that reported by King et al. (2016a), and thus such trends may be masked by measurement uncertainties. In common with previous studies that have used this modelling approach, values of E_t are lower than those obtained via emission spectroscopy (e.g., see Riedesel et al., 2019 for a summary), which is a consequence of E_t, E_u and s trading off with one another during data fitting.

Rates of anomalous fading generally reduce with increasing stimulation temperature. Fading rates are similar between samples from the same study site with the exception of sample KTB.253F that has much higher fading rates than the other samples from the KTB borehole, and exhibits an increase in g_{2d} values with increasing measurement temperature. Whereas the D_e values reduce with depth because of increasing temperature for the KTB samples, the D_e values are similar between the different surface samples of the Butwal transect.

Table 4
$\tilde{n}_{mod}(end)$ values for the elevated temperature irradiation experiments. Irradiation was done for 24 h, with instrument dose rate of $\dot{D}_{lab} \approx (3.627 \pm 0.095) \times 10^9$ Gy/ka $= 0.116 \pm 0.003$ Gy/s for sample BUT.4, and $\dot{D}_{lab} \approx (3.595 \pm 0.095) \times 10^9$ Gy/ka $= 0.114 \pm 0.003$ Gy/s for sample KTB.428B.

Sample	Irradiation temperature [°C]	$\tilde{n}_{mod}$ (end) IRSL.50	$\tilde{n}_{mod}$ (end) IRSL.100	$\tilde{n}_{mod}$ (end) IRSL.150	$\tilde{n}_{mod}$ (end) IRSL.225
BUT.4	200 °C	0.655	0.764	0.828	0.880
	250 °C	0.211	0.335	0.462	0.638
	300 °C	0.018	0.038	0.073	0.182
KTB.428B	250 °C	0.189	0.389	0.376	0.361

3.2. Inversion for isothermal temperature

3.2.1. KTB borehole: known-temperature samples

The results of the temperature inversion using different ITL combinations for the KTB samples are presented in Fig. 4. The difference

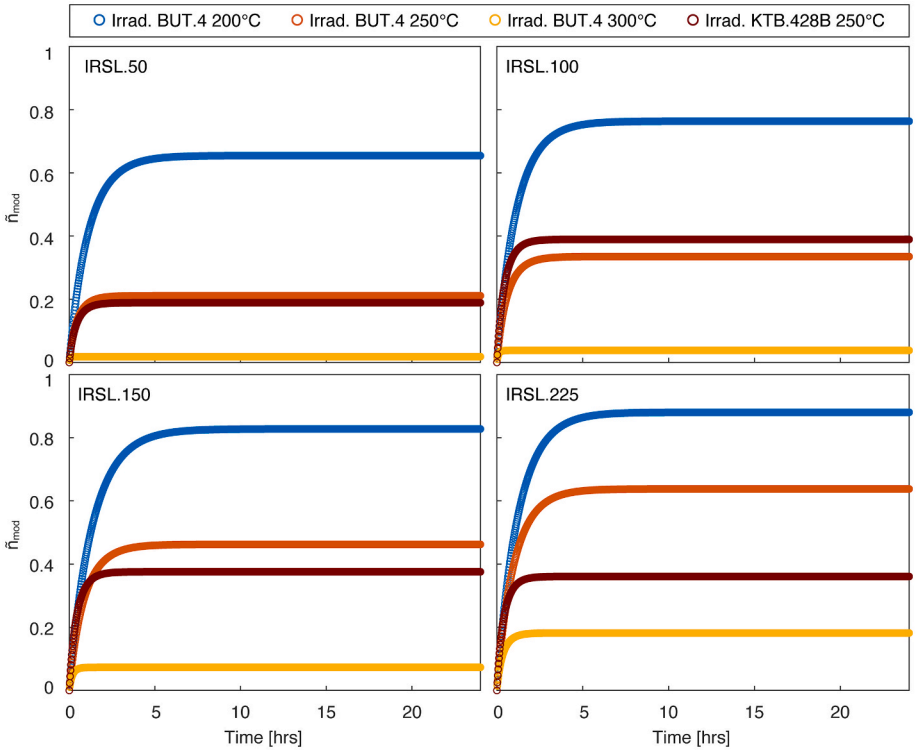

Fig. 2. Evolution of $\tilde{n}_{mod}$ values for the elevated temperature irradiation experiments. See caption of Table 4 for the irradiation conditions.

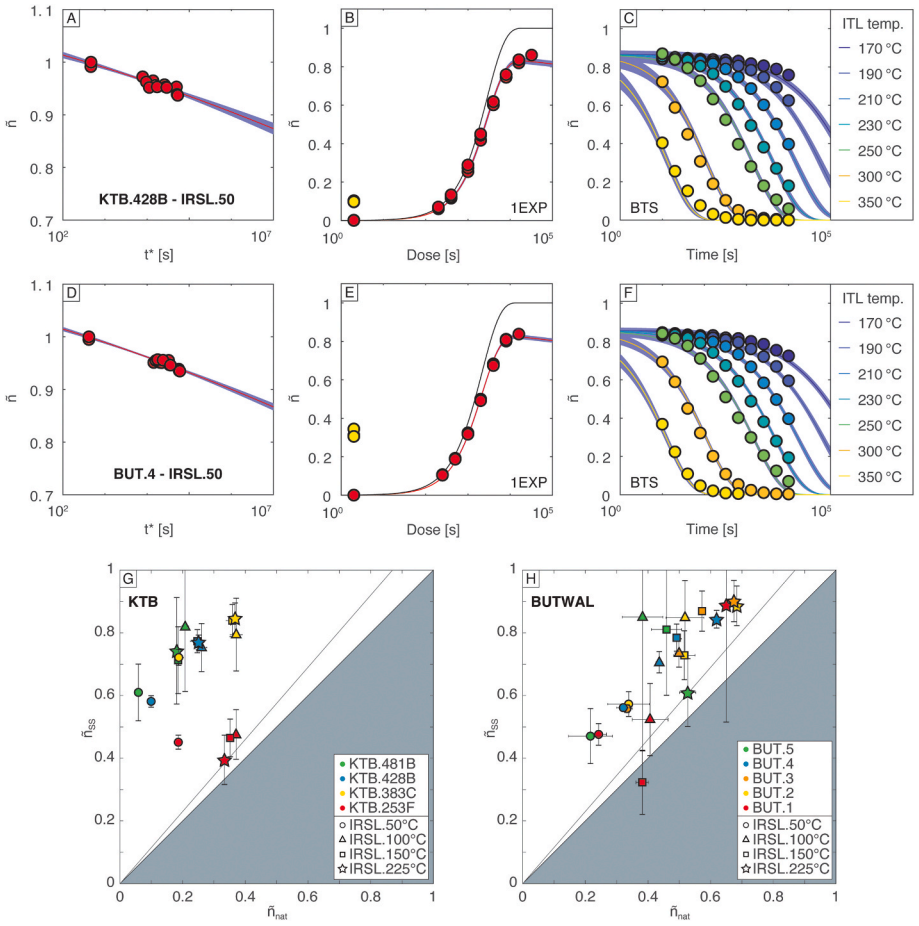

Fig. 3. Luminescence measurement and model fit results for the IRSL.50 signal of one KTB and one Butwal sample. (A, D) Anomalous fading data fitted using Eq. (3) and (4). (B, E) Luminescence dose response corrected for fading, fitted using Eq. (5). The black solid line is the unfaded dose response curve, and the yellow dots represent the $\tilde{n}_{nat}$ values of each aliquot. (C, F) Isothermal decay data fitted with the BTS model, using Eq. (6) and (7). (G, H) Saturation plots (Kars plots) contrasting natural luminescence values, $\tilde{n}_{nat}$, with steady-state luminescence values, $\tilde{n}_{SS}$, predicted for each of the KTB and Butwal samples. The 1:1 line delimits saturated samples (grey area) to unsaturated samples (white area), with the saturation limit indicated by the grey line.

Table 5
Summary of kinetic and fitted parameters of the KTB and Butwal samples, for all four IRSL temperatures, using kinetic parameters derived from four isothermal temperatures between 190 and 250 °C. Uncertainties are listed at 1σ for all values, except for D_e, for which errors are listed as 5 % of D_e. Fading rates are expressed both as ρ' and as g-values normalised to 2 days, g_{2d}, Huntley and Lamothe (2001).

Sample/IRSL		E_t [eV]	E_u [eV]	$\log_{10} s$ [s^{-1}]	$\log_{10}$ ρ' [-]	g_{2d} [%/dec.]	D_e [Gy]	D_0 [Gy]	$\tilde{n}_{nat}$ [-]
KTB.253F	50	1.58 ± 0.06	0.08 ± 0.01	11.83 ± 0.58	−5.55 ± 0.03	3.73 ± 0.24	197 ± 10	389 ± 14	0.19 ± 0.01[a]
	100	1.63 ± 0.11	0.10 ± 0.01	11.85 ± 1.08	−5.57 ± 0.10	3.67 ± 0.81	336 ± 17	235 ± 7	0.37 ± 0.01
	150	1.61 ± 0.10	0.09 ± 0.01	11.81 ± 1.01	−5.56 ± 0.07	3.87 ± 0.65	330 ± 17	247 ± 9	0.35 ± 0.01
	225	1.60 ± 0.09	0.10 ± 0.01	11.74 ± 0.93	−5.47 ± 0.09	4.50 ± 0.97	364 ± 18	210 ± 9	0.33 ± 0.01
KTB.383C	50	1.57 ± 0.06	0.08 ± 0.01	11.58 ± 0.56	−5.92 ± 0.04	1.62 ± 0.17	96 ± 5	326 ± 12	0.19 ± 0.02
	100	1.63 ± 0.08	0.09 ± 0.01	11.75 ± 0.81	−6.06 ± 0.23	1.21 ± 0.63	126 ± 6	204 ± 7	0.37 ± 0.02
	150	1.62 ± 0.09	0.09 ± 0.01	11.65 ± 0.86	−6.18 ± 0.13	0.92 ± 0.28	120 ± 6	218 ± 8	0.36 ± 0.02
	225	1.58 ± 0.08	0.09 ± 0.01	11.35 ± 0.79	−6.20 ± 0.13	0.89 ± 0.27	111 ± 6	198 ± 6	0.37 ± 0.01
KTB.428B	50	1.61 ± 0.06	0.08 ± 0.01	11.93 ± 0.54	−5.71 ± 0.02	2.62 ± 0.15	100 ± 5	552 ± 17	0.10 ± 0.01[a]
	100	1.64 ± 0.08	0.09 ± 0.01	11.88 ± 0.81	−5.98 ± 0.14	1.44 ± 0.46	135 ± 7	323 ± 10	0.26 ± 0.02
	150	1.61 ± 0.08	0.08 ± 0.01	11.68 ± 0.73	−6.02 ± 0.08	1.31 ± 0.22	126 ± 6	333 ± 11	0.25 ± 0.02
	225	1.62 ± 0.07	0.08 ± 0.01	11.81 ± 0.67	−6.01 ± 0.05	1.35 ± 0.15	120 ± 6	308 ± 10	0.25 ± 0.02
KTB.481B	50	1.55 ± 0.06	0.08 ± 0.01	11.16 ± 0.60	−5.75 ± 0.12	2.39 ± 0.68	52 ± 3	531 ± 21	0.06 ± 0.01[a]
	100	1.60 ± 0.08	0.09 ± 0.01	11.29 ± 0.77	−6.13 ± 0.39	1.02 ± 0.93	79 ± 4	275 ± 9	0.21 ± 0.01
	150	1.58 ± 0.08	0.09 ± 0.01	11.16 ± 0.75	−5.90 ± 0.17	1.72 ± 0.68	83 ± 4	282 ± 10	0.19 ± 0.01[a]
	225	1.59 ± 0.07	0.09 ± 0.01	11.32 ± 0.71	−5.95 ± 0.27	1.51 ± 0.95	77 ± 4	279 ± 13	0.18 ± 0.01[a]
BUT.5	50	1.38 ± 0.08	0.10 ± 0.01	9.04 ± 0.80	−5.58 ± 0.11	3.47 ± 0.84	459 ± 23	781 ± 28	0.22 ± 0.07
	100	1.50 ± 0.07	0.09 ± 0.01	9.96 ± 0.69	−6.24 ± 0.73	0.80 ± 1.30	385 ± 19	650 ± 27	0.38 ± 0.06
	150	1.42 ± 0.08	0.08 ± 0.01[a]	8.69 ± 0.72	−6.13 ± 0.39	1.04 ± 0.91	543 ± 27	659 ± 25	0.46 ± 0.05
	225	1.66 ± 0.08	0.09 ± 0.01[a]	10.55 ± 0.79	−5.76 ± 0.14	2.39 ± 0.79	1080 ± 54	561 ± 24	0.53 ± 0.03
BUT.4	50	1.54 ± 0.06	0.08 ± 0.01	11.20 ± 0.60	−5.68 ± 0.01	2.78 ± 0.10	361 ± 18	442 ± 9	0.32 ± 0.02
	100	1.52 ± 0.06	0.08 ± 0.01[a]	10.74 ± 0.53	−5.90 ± 0.06	1.70 ± 0.23	399 ± 20	426 ± 10	0.44 ± 0.01
	150	1.51 ± 0.06	0.08 ± 0.01[a]	10.24 ± 0.59	−6.06 ± 0.09	1.22 ± 0.26	473 ± 24	489 ± 13	0.49 ± 0.01
	225	1.53 ± 0.06	0.08 ± 0.01[a]	9.95 ± 0.54	−6.21 ± 0.08	0.85 ± 0.16	569 ± 28	436 ± 14	0.62 ± 0.02
BUT.3	50	1.53 ± 0.06	0.09 ± 0.01	10.90 ± 0.59	−5.68 ± 0.02	2.79 ± 0.11	419 ± 21	480 ± 16	0.33 ± 0.02
	100	1.55 ± 0.06	0.08 ± 0.01[a]	10.96 ± 0.57	−5.95 ± 0.08	1.51 ± 0.28	421 ± 21	378 ± 11	0.50 ± 0.01
	150	1.47 ± 0.06	0.07 ± 0.01[a]	9.92 ± 0.57	−6.29 ± 0.19	0.69 ± 0.31	441 ± 22	414 ± 14	0.57 ± 0.01
	225	1.50 ± 0.06	0.08 ± 0.01[a]	9.59 ± 0.59	−6.42 ± 0.24	0.52 ± 0.29	499 ± 25	365 ± 15	0.67 ± 0.01
BUT.2	50	1.54 ± 0.06	0.08 ± 0.01[a]	10.45 ± 0.54	−5.70 ± 0.05	2.64 ± 0.32	472 ± 24	548 ± 19	0.34 ± 0.07
	100	1.55 ± 0.09	0.08 ± 0.01	10.33 ± 0.82	−6.23 ± 0.28	0.83 ± 0.54	392 ± 20	419 ± 16	0.52 ± 0.06
	150	1.56 ± 0.10	0.07 ± 0.01	10.47 ± 0.97	−5.94 ± 0.13	1.54 ± 0.48	522 ± 26	432 ± 18	0.52 ± 0.03
	225	1.60 ± 0.10	0.08 ± 0.01	10.48 ± 0.93	−6.36 ± 0.21	0.60 ± 0.29	492 ± 25	336 ± 17	0.68 ± 0.02
BUT.1	50	1.43 ± 0.07	0.09 ± 0.01	9.44 ± 0.64	−5.58 ± 0.04	3.47 ± 0.34	425 ± 21	626 ± 20	0.24 ± 0.03
	100	1.56 ± 0.16	0.08 ± 0.01	10.66 ± 1.54	−5.63 ± 0.14	3.12 ± 1.02	658 ± 33	459 ± 24	0.41 ± 0.06
	150	1.59 ± 0.17	0.09 ± 0.01	10.77 ± 1.61	−5.39 ± 0.12	5.48 ± 1.54	1385 ± 66	407 ± 19	0.38 ± 0.02
	225	1.46 ± 0.11	0.08 ± 0.01	9.29 ± 0.99	−6.37 ± 0.75	0.59 ± 1.02	419 ± 21	322 ± 15	0.65 ± 0.01

[a] Uncertainty <0.005.

between the predicted temperature values and the in-situ temperature values for the KTB samples studied can be used to assess which ITL combination should be used to yield reliable thermal histories.

Different ITL combinations yield different inverted temperatures. The higher the end-temperature of the ITL combination, the lower the modelled temperature. When the ITL data for temperatures of 300 or 350 °C are included, or if all seven isothermal holding temperatures are used, the KTB borehole temperatures are not recovered, even within error (grey areas in Fig. 4).

3.2.2. Butwal transect: unknown-temperature samples

The K-feldspar samples of the Butwal transect have no independent temperature control and were collected at the surface, from bedrock outcrops. Their inversion for ambient temperature (Fig. 5) might not reflect the thermal reality of the sample and rather than reflecting surface temperature, it may relate to the cooling history experienced by these rocks.

For the Butwal samples (Fig. 5), there is less variation in the inverted temperatures with different combinations of ITL temperatures, relative to the KTB samples (Fig. 4). All of the inversions give modelled temperatures below 60 °C, with an average for all the ITL combinations of around 30–35 °C. Visible exceptions are the IRSL.100 signal of sample BUT.1, and the IRSL.50 signal of sample BUT.5, that give inverted temperatures around 20 °C, ~10–15 °C below the results of the other samples and IRSL signals.

3.2.3. Control samples: unknown-temperature samples

The twelve control samples have a range of trapped charge concentrations. As the natural trapped charge concentration partly controls the inverted temperatures, all inverted temperatures were normalised to an average value to facilitate comparison (Fig. 6). This was done by fitting the data with a linear regression and by moving the origin of the regression lines to the same initial temperature.

Despite their difference in mineralogy and lithology, the samples generally depict the same trend: a decrease in inverted temperature with the inclusion of higher temperature ITL data (Fig. 6). For most samples, there is a change in behaviour in the data when the final temperature of the ITL combination passes from 250 °C to 300 °C. The scatter between the different inverted temperatures increases, and the inverted temperatures generally reduce (Fig. 6). Although affected by this trend, the K-feldspar samples seem to exhibit less variation in inverted temperature between different ITL data combinations than the Na-feldspar samples. These results are consistent with that recorded for the Butwal and KTB samples (Figs. 4–6).

3.2.4. Synthetic calibration samples: high temperature irradiations

In contrast to the natural samples, inversion of the laboratory high-temperature irradiation data for both sample BUT.4 and sample KTB.428B exhibited less sensitivity to the different combinations of ITL data (left-hand side of Fig. 7, and Table 6).

All of the ITL combinations recover the irradiation temperature within 10 % error of the target temperature, however, only the 250 °C irradiation of sample BUT.4 recovers the irradiation temperature exactly with all of the IRSL signals (Table 6). For the 250 °C irradiation of sample KTB.428B, and the 300 °C irradiation of sample BUT.4, there is a consistent underestimation of the modelled temperature compared to

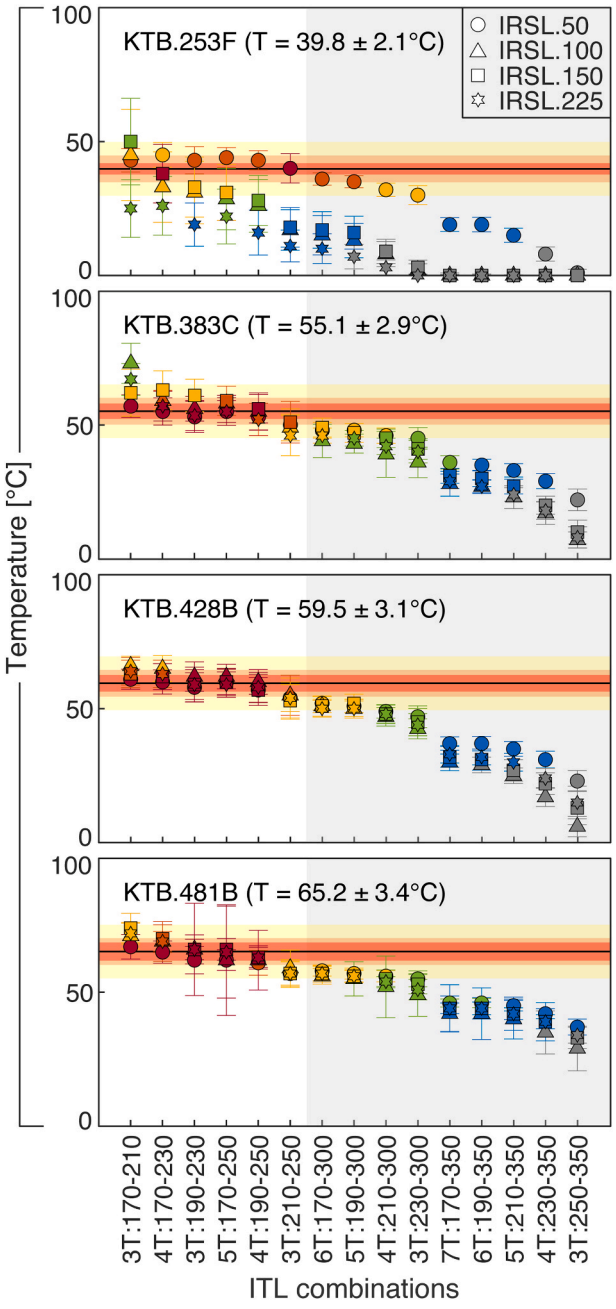

Fig. 4. Results of the inversion for isothermal temperatures for the KTB borehole samples. Different combinations of ITL temperatures are tested. The different colours represent how close the inverted temperatures are to the target in-situ temperature. The red area and the red dots are modelled temperatures within the error range of the in-situ temperature, the orange area and dots are within 5 °C of the target-temperature, and the yellow area and dots are within 10 °C of the target-temperature. The green dots have a difference of 10–20 °C with the in-situ temperature, 20–30 °C for the blue dots, and above 30 °C for the grey dots. The solid black line is the target in-situ temperature, and the red-coloured areas represent the error on this temperature. The grey area highlights the ITL combinations that do not successfully recover the in-situ temperature of the KTB borehole, within error.

the target temperature of ~15 and ~20 °C (~15–25 °C depending on the IRSL signal) respectively (Table 6). For the 200 °C irradiation of sample BUT.4, only the IRSL.150 perfectly recovers the target-temperature. The IRSL.225 signal shows an underestimation of ~40 °C (Table 6), and the IRSL.50 and 100 signals overestimate the temperature by ~5–15 °C, but all signals recover the target-temperature within 1σ error.

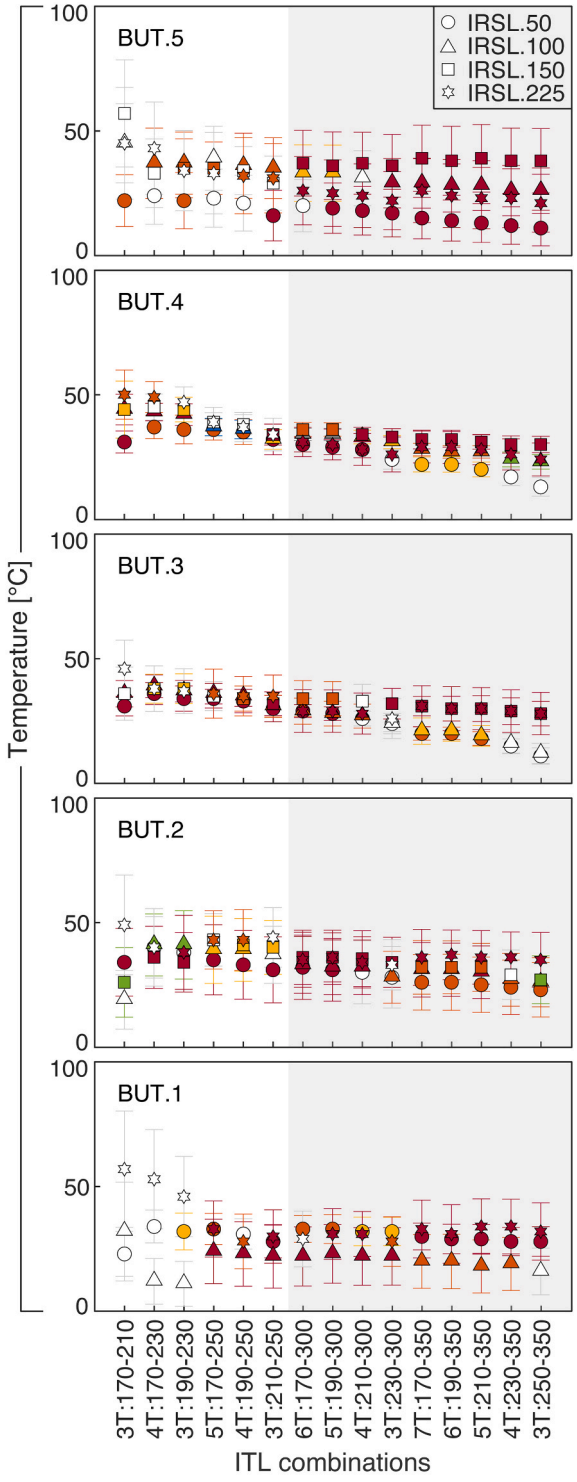

Fig. 5. Results of the inversion for isothermal temperatures for the Butwal samples. The IRSL.150 signal of sample BUT.1 is not included in the results as this signal is in saturation ($\tilde{n}_{nat} > \tilde{n}_{SS}$, see Fig. 3H, and $D_e > 2D_0$, see Table 5). Different combinations of ITL temperatures are tested. The different colours represent different temperature plateaux identified using a nearest neighbour Matlab cluster function, that regroups temperatures by how close they are to each other, independent of their position on the x-axis. The largest plateaux are in red (then orange, yellow, green, blue, and grey). White data points are ITL combinations for which there is no plateau (only one data point yields this temperature).

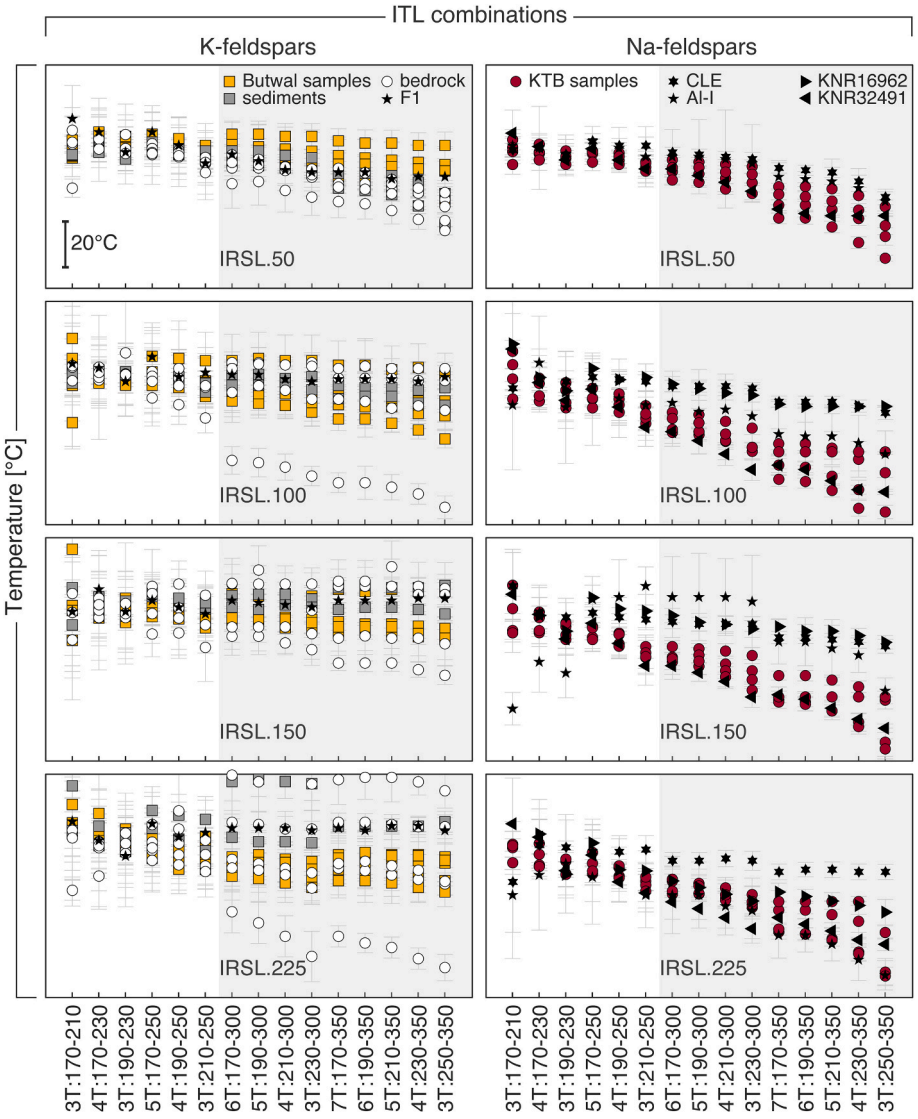

Fig. 6. Normalised results of the inversion of the control samples, the KTB and Butwal samples. Samples details are given in Table 3. The IRSL signals which are in saturation ($\widetilde{n}_{nat} > \widetilde{n}_{SS}$, see Supplementary material S5, Fig. S5) are not included in the results. Note that the data have been aligned on the y-axis, despite reflecting different thermal histories, to allow the data trends to be contrasted.

When the data are inverted using the natural environmental dose rate (right-hand side of Fig. 7, and Table 6), they are again sensitive to the combination of ITL temperatures used and exhibit a similar trend to that observed for the naturally irradiated samples (Figs. 4 and 5), with sample KTB.428B exhibiting the greatest sensitivity. Despite this, irradiation at 250 °C for both samples yields inverted temperatures of around ~40–45 °C for all ITL combinations when ITL data measured at 300 and 350 °C are excluded. The irradiation at 300 °C gives an approximate temperature in the range of 55–60 °C, and the lowest temperature of irradiation at 200 °C has a natural equivalent below 20 °C, even reaching temperatures below 0 °C depending on the ITL combination, indicating that the sample would likely be in steady-state in the natural environment. With the exception of the irradiation at 200 °C that yields an equivalently saturated result, the other high temperature irradiations correspond to physically possible temperatures in nature and are in the range of the temperatures recorded for the KTB samples.

4. Discussion

Samples with independently known thermal histories provide an opportunity to validate measurement and modelling approaches relevant for luminescence thermochronometry. Here we use samples from the KTB borehole, together with synthetically developed known-thermal history samples, to test the validity of thermal kinetic parameters obtained from different combinations of isothermal holding data. We find that inverted temperatures change, depending both on the number of ITL temperatures and on the highest ITL temperature used for thermal kinetic parameter derivation (Figs. 4–7). Modelled temperatures reduce as the highest ITL temperature increases, to the extent that the KTB borehole sample temperatures are no longer recovered when the 300 and 350 °C ITL are included to derive the thermal kinetic parameters. Only where these temperatures are excluded are the KTB borehole sample temperatures recovered accurately. The temperature deviation observed when the 300 and 350 °C ITL temperatures are incorporated might be explained by enhanced thermal transfer of charges at temperatures greater than the preheat temperature (King et al., 2016a; Lambert, 2018), which was 250 °C for all of the analyses reported here. The observation that the 300 and 350 °C ITL data are least well fitted by the band-tail states model (Fig. 3C and 3F), is consistent with this result. Where the 300 and 350 °C ITL temperatures are excluded, all of the data combinations between three and five ITL temperatures between 170 °C

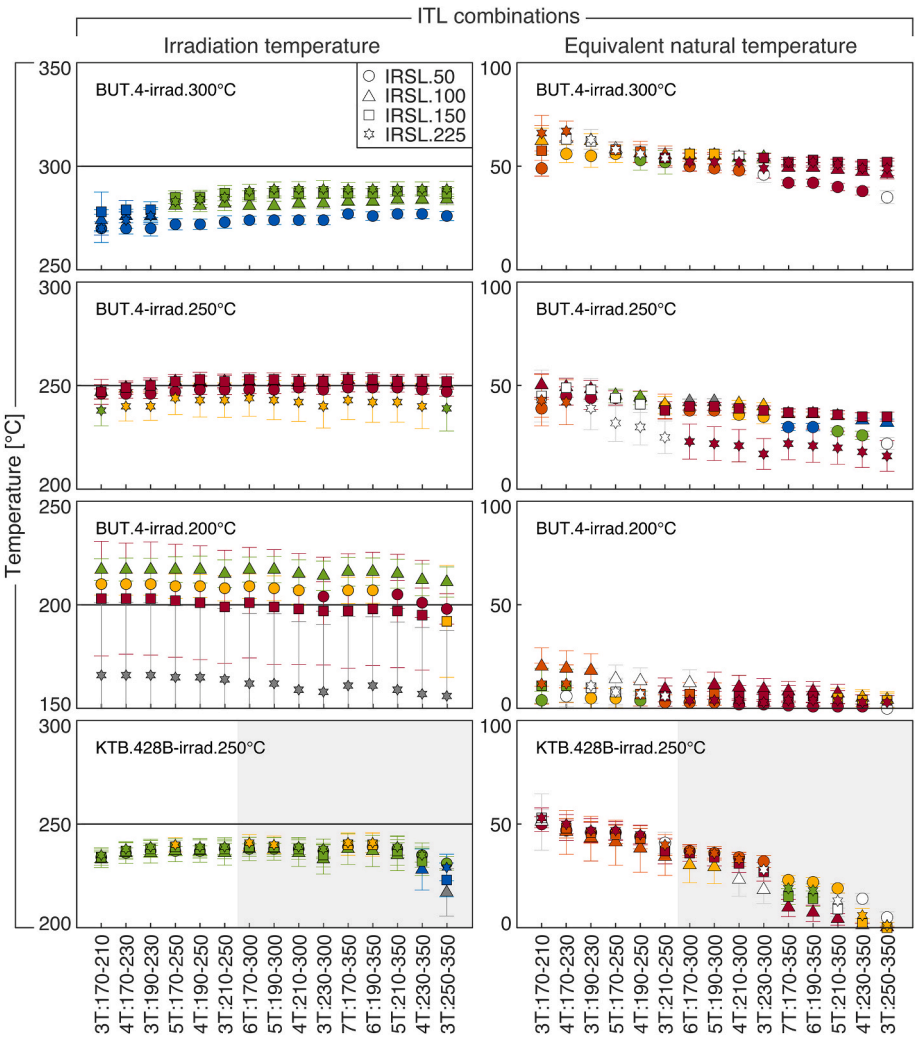

Fig. 7. On the left-hand side, results of the inversion for isothermal temperatures for the high temperature irradiation measurements on K-feldspar sample BUT.4 and Na-feldspar sample KTB.428B. Solid black lines are the irradiation target temperatures. On the right-hand side, results of inversion of the high temperature irradiation data using the natural environmental dose rate. For the definition of the colours, refer to the caption of Fig. 5.

and 250 °C yield accurate in-situ temperatures for the KTB samples (Fig. 4).

However, the KTB borehole samples are Na-feldspar, whereas K-feldspar is usually targeted in luminescence studies because of its favourable luminescence dating properties (i.e. brighter signal intensities). The Butwal samples are K-feldspars and their response to changing ITL temperature combinations (Fig. 5) is somewhat different to that observed for the KTB samples (Fig. 4). Although it is not known whether the Butwal samples reflect exhumation or isothermal temperature, inverting the samples assuming an isothermal history is useful for exploring the effect of different thermal kinetic parameters obtained from different ITL combinations. It is apparent from contrasting Figs. 4 and 5 that whereas the KTB samples exhibit high sensitivity to the combination of ITL temperatures, and in particular the inclusion of highest temperature ITL measurements, that the Butwal samples are relatively unaffected. Although there is a trend towards reducing temperature and increasing scatter between the different MET signals with the inclusion of higher temperature ITL data (Fig. 6), the temperature change is more moderate, especially for samples BUT.2, BUT.3 and BUT.4 which are far from saturation (Fig. 3H). In contrast, the data for BUT.1 and BUT.5 is more scattered, which may reflect the higher saturation level of at least one of the MET signals of these samples.

This difference in behaviour between the Na-feldspars of the KTB samples and the K-feldspars of the Butwal samples is also seen in the control feldspars (Fig. 6). Despite their difference in mineralogy and lithology, all samples generally depict the same trend, with a decrease in inverted temperature with the inclusion of the highest temperature ITL data. The scatter between the different inverted temperatures also increases when the 300 and 350 °C ITL data are included (Fig. 6). The K-feldspars (left-side of Fig. 6) are generally less affected than Na-feldspars (right-side of Fig. 6), with some exceptions. Sample lithology appears to be a controlling factor, with sedimentary samples exhibiting the least sensitivity to changing ITL combinations. However, the most significant trend is between samples from the same location. The KTB samples exhibit similar behaviour, clearly distinguishable from the other Na-feldspars, and the Butwal samples are similar to each other but distinguishable from the other K-feldspars.

The differences in inverted temperatures discussed above illustrate the importance of identifying a suitable measurement protocol. If we isolate the ITL combination that gives the most consistent results, i.e., where independently known temperature is recovered (Fig. 4) and the scatter between the data is the least (Figs. 4 and 6), based on the results of the KTB borehole samples, we are left with one combination of four isothermal temperatures between 190 and 250 °C. However, in most geological applications, independent temperature control is absent, and it is thus usually not possible to select which of these ITL temperature combinations yields the most accurate result. For this reason, we sought to develop synthetic calibration samples through elevated temperature

Table 6
Average modelled temperatures, and their standard error, for each individual IRSL signal, and for all IRSL signals together, for A. the elevated temperature irradiation experiments, with $\dot{D}_{lab}$, and B. their equivalent natural temperature, with $\dot{D}_{nat}$.

A	Sample	Average modelled temperatures [°C], $\dot{D}_{lab}$				
		IRSL.50	IRSL.100	IRSL.150	IRSL.225	All IRSL
	BUT.4-irrad300°C	274 ± 3	281 ± 3	285 ± 3	285 ± 6	281 ± 6
	BUT.4-irrad250°C	248 ± 1	251 ± 2	252 ± 2	242 ± 2	248 ± 4
	BUT.4-irrad200°C	207 ± 3	216 ± 2	199 ± 3	162 ± 3	196 ± 21
	KTB.428B-irrad250°C	237 ± 2	234 ± 5	236 ± 4	238 ± 3	236 ± 4
B	Sample	Average modelled temperatures [°C], $\dot{D}_{nat}$				
		IRSL.50	IRSL.100	IRSL.150	IRSL.225	All IRSL
	BUT.4-irrad300°C	47 ± 7	54 ± 6	56 ± 4	55 ± 6	53 ± 6
	BUT.4-irrad300°C *	54 ± 3	59 ± 3	59 ± 3	61 ± 5	58 ± 5
	BUT.4-irrad250°C	36 ± 7	41 ± 6	40 ± 4	26 ± 9	36 ± 9
	BUT.4-irrad250°C *	43 ± 2	46 ± 4	44 ± 4	35 ± 7	42 ± 6
	BUT.4-irrad200°C	3 ± 2	11 ± 5	7 ± 2	6 ± 3	7 ± 4
	BUT.4-irrad200°C *	5 ± 1	16 ± 4	9 ± 2	9 ± 3	10 ± 5
	KTB.428B-irrad250°C	33 ± 14	25 ± 17	29 ± 17	32 ± 17	30 ± 16
	KTB.428B-irrad250°C *	46 ± 3	42 ± 6	45 ± 5	47 ± 4	45 ± 5

Note: Data with * are calculated without the ITL combinations including the ITL temperatures at 300 and 350 °C.

irradiation in the laboratory (e.g., Wallinga et al., 2002).

In contrast to the naturally irradiated samples, inversion of the elevated temperature irradiated samples reveals almost no sensitivity to the number of ITL temperatures incorporated (left-hand side of Fig. 7, and Table 6). Inverting these data again, instead using the sample's respective natural dose rate (right-hand side of Fig. 7, and Table 6), reveals that the laboratory dose rate masks the effect of changes in the thermal kinetic parameters. The laboratory dose rate of our instrument is nine orders of magnitude greater than the natural environmental dose rate. The rate of charge accumulation is thus disproportionally high in comparison to the lifetime of charges in the traps, which is defined by the sample's thermal kinetic parameters. Consequently, relatively little charge is thermally evicted compared to the rate of charge trapping, and variation in the thermal kinetic parameters caused by the differences in ITL combinations (left-hand side of Fig. 7) has almost no impact. In contrast, the natural environment is much more sensitive to these subtle changes in kinetic parameters (Figs. 4 and 5 and right-hand side of Fig. 7) because of the comparatively slow rate of charge trapping relative to charge detrapping.

It is thus challenging to develop highly sensitive luminescence thermochronometry calibration samples in the laboratory. Despite this, we recover the irradiation temperatures within error for all of our experiments indicating that our measurement and modelling approach is robust. The large uncertainties recorded for the 200 °C irradiation of the IRSL.225 signal of sample BUT.4 reflect the fact that the $\tilde{n}_{synth.lab}$ values are near to saturation for this irradiation temperature, preventing the recovery of a precise thermal history. For the 250 °C irradiation of KTB.428B and the 300 °C irradiation of BUT.4, the modelled temperature slightly underestimates the measured temperatures (Table 6). This may partly relate to small deviations between the heating temperature prescribed in the measurement sequence, and that experienced by the sample disc. Despite this, as the modelled results are within 10 % uncertainty of the measured value, we consider the results to be robust.

As the synthetic calibration data are not sufficiently sensitive to aid in the selection of an appropriate combination of ITL temperatures, we instead contrasted the results of inverting both the natural data for the KTB and Butwal samples (Figs. 4 and 5) and the inversion of the elevated temperature irradiation data using the natural environmental dose rate (right-hand side of Fig. 7). For the inversion of the natural KTB data, kinetic parameters calculated from four ITL temperatures between 190 and 250 °C recover the in-situ temperature both accurately and precisely for all samples and all IRSL signals, with the exception of the post-IR signals of sample KTB.253F. This sample has a different lithology to the other KTB samples analysed, comprising garnet-amphibolite, rather than biotite-gneiss, and it exhibits higher rates of anomalous fading (Table 5). Consequently, the post-IR $\tilde{n}_{nat}$ values for this samples are close to saturation (Fig. 3G), which limits their ability to recover its thermal history. The combination of four ITL temperatures also yields tightly clustered inversion results for the natural samples BUT.2, BUT.3 and BUT.4 (Fig. 5), although the data are more scattered for BUT.1 and BUT.5. As the latter two samples have at least one IRSL signal saturated or near to saturation (Fig. 3H), we do not discard this temperature combination on their account. Similarly, this combination of ITL temperatures yields accurate results for the elevated irradiation temperature data (left-hand side of Fig. 7), and tightly clustered results for the inversion of these data using the natural environmental dose rate (right-hand side of Fig. 7). For this reason, we consider this combination of temperatures as appropriate for both the KTB and Butwal samples. But in the absence of known-thermal history samples for K-feldspars, we acknowledge that this combination of temperatures may not yield accurate results for the Butwal samples.

5. Conclusions

In this study, the impact of different combinations of isothermal holding temperature data was investigated in the context of luminescence thermochronometry, using a combination of numerical modelling and experimental data. Measurement of Na-feldspar minerals from known-thermal history KTB borehole samples allowed validation of the MET-pIR-IRSL measurement protocol for luminescence thermochronometry through the successful recovery of in-situ borehole temperatures. However, these samples also showed that the inclusion of isothermal holding data above 250 °C resulted in kinetic parameters that underestimated temperature. As the majority of luminescence studies are applied to K-feldspar minerals, complimentary investigations on unknown thermal history K-feldspar minerals extracted from samples of the Nepalese Siwaliks (Butwal transect) were made. These experiments yielded similar results, although these samples were notably less sensitive to the inclusion of isothermal holding data above 250 °C, whilst also exhibiting a trend of reducing inverted temperature with the inclusion of higher temperature isothermal data. To evaluate how representative the KTB and Butwal samples are of K-feldspar and Na-feldspars generally, we contrasted our data with a suite of twelve control samples of different chemical compositions and geological origins. The most distinctive trend is that samples from the same locality tend to exhibit similar behaviour, and that most samples yield lower reconstructed temperatures where high temperature isothermal holding data are used for kinetic parameter derivation.

Finally, we attempted to develop artificial luminescence calibration samples in the laboratory, through irradiating a K-feldspar (BUT) and Na-feldspar (KTB) sample at elevated temperature. However, the laboratory dose rate is nine orders of magnitude greater than that experienced in nature and masked the effect of changes in the kinetic parameters caused by their calculation with different sub-sets of isothermal data. Consequently, through consideration of the trends in all

of our data, and in particular the isothermal temperature combination that yielded the most accurate in-situ temperatures for the KTB borehole samples, we advocate using four isothermal temperatures at 190, 210, 230 and 250 °C to determine thermal kinetic parameters from isothermal holding experiments. We find that this temperature combination performed accurately for the four MET signals investigated for the KTB samples, and that the decline in inverted temperatures occurred when isothermal decay data above 250 °C were incorporated. However, we acknowledge that in the absence of any independent control on sample thermal history, this may still yield inaccurate results for some feldspar minerals. Generating locality specific plots that explore changes in inverted temperatures for a sub-set of samples using different combinations of isothermal holding temperature data will allow the sensitivity of a sample to be analysed and the selected measurement conditions to be at least partially evaluated.

Declaration of competing interest

The authors declare that they have no known competing financial interests or personal relationships that could have appeared to influence the work reported in this paper.

Acknowledgements

The authors would like to thank A. Finch for providing the sample CLE, H. Friis and the Natural History Museum of Oslo for the KNR16962 and KNR32491 samples, B. Guralnik for the KTB samples, J. Lavé for the Butwal samples, and S. Riedesel for measuring the samples AL-I, HAM-5 and JSH1-13. The authors would also like to thank M. Bartz, S. Riedesel, S. Tsukamoto and F. Oppermann for laboratory support, and F. Herman and C. Schmidt for comments and suggestions on the manuscript. G.E. King has received funding from the European Research Council (ERC) under the European Union's Horizon 2020 research and innovation programme, grant agreement No. 851614. Comments from Eren Şahiher and an anonymous reviewer improved the manuscript.

Appendix A. Supplementary data

Supplementary data to this article can be found online at https://doi.org/10.1016/j.quageo.2021.101240.

References

Auclair, M., Lamothe, M., Huot, S., 2003. Measurement of anomalous fading for feldspar IRSL using SAR. Radiat. Meas. 37, 487–492.
Ault, A.K., Gautheron, C., King, G.E., 2019. Innovations in (U–Th)/He, fission track, and trapped charge thermochronometry with applications to earthquakes, weathering, surface-mantle connections, and the growth and decay of mountains. Tectonics 38 (11), 3705–3739.
Balescu, S., Lamothe, M., 1994. Comparison of TL and IRSL age estimates of feldspar coarse grains from waterlain sediments. Quat. Sci. Rev. 13, 437–444.
Biswas, R.H., Herman, F., King, G.E., Braun, J., 2018. Thermoluminescence of feldspar as a multi-thermochronometer to constrain the temporal variation of rock exhumation in the recent past. Earth Planet Sci. Lett. 495, 56–68.
Biswas, R.H., Herman, F., King, G.E., Lehmann, B., Singhvi, A.K., 2020. Surface paleothermometry using low-temperature thermoluminescence of feldspar. Clim. Past 16 (6), 2075–2093.
Brennan, B.J., Lyons, R.G., Phillips, S.W., 1991. Attenuation of alpha particle track dose for spherical grains. Int. J. Radiat. Appl. Instrum. Nucl. Tracks Radiat. Meas. 18 (1–2), 249–253.
Brown, N.D., Rhodes, E.J., Harrison, T.M., 2017. Using thermoluminescence signals from feldspars for low-temperature thermochronology. Quat. Geochronol. 42, 31–41.
Buscombe, D., 2013. Transferable wavelet method for grain-size distribution from images of sediment surfaces and thin sections, and other natural granular patterns. Sedimentology 60, 1709–1732.
Coyle, D.A., Wagner, G.A., Hejl, E., Brown, R., Van den Haute, P., 1997. The cretaceous and younger thermal history of the KTB site (Germany) apatite fission-track data from the Vorbohrung. Geol. Rundsch. 86, 203–209.
Durcan, J.A., King, G.E., Duller, G.A.T., 2015. DRAC: dose rate and age calculator for trapped charge dating. Quat. Geochronol. 28, 54–61.
Gautam, P., Apple, E., 1997. Magnetic-polarity stratigraphy of Siwalik Group sediments of Tinau Khola section in west central Nepal, revisited. Geophys. J. Int. 117, 223–234.
Guérin, G., Mercier, N., Adamiec, G., 2011. Dose-rate conversion factors: update. Ancient TL 29 (1), 5–8.
Guérin, G., Mercier, N., Nathan, R., Adamiec, G., Lefrais, Y., 2012. On the use of the infinite matrix assumption and associated concepts: a critical review. Radiat. Meas. 47, 778–785.
Guralnik, B., Jain, M., Herman, F., Paris, R.B., Harrison, T.M., Murray, A.S., Valla, P.G., Rhodes, E.J., 2013. Effective closure temperature in leaky and/or saturating thermochronometers. Earth Planet Sci. Lett. 384, 209–218.
Guralnik, B., Li, B., Jain, M., Chen, R., Paris, R.B., Murray, A.S., Li, S.-H., Pagonis, V., Valla, P.G., Herman, F., 2015a. Radiation-induced growth and isothermal decay of infrared-stimulated luminescence from feldspar. Radiat. Meas. 81, 224–231.
Guralnik, B., Jain, M., Herman, F., Ankjærgaard, C., Murray, A.S., Valla, P.G., Preusser, F., King, G.E., Chen, R., Lowick, S.E., Kook, M., Rhodes, E.J., 2015b. OSL-thermochronology of feldspar from the KTB borehole, Germany. Earth Planet Sci. Lett. 423, 232–243.
Herman, F., King, G.E., 2018. Luminescence thermochronometry: investigating the link between mountain erosion, tectonics and climate. Elements 14, 33–38.
Herman, F., Copeland, P., Avouac, J.-P., Bollinger, L., Mahéo, G., Le Fort, P., Rai, S., Foster, D., Pêcher, A., Stüwe, K., Henry, P., 2010. Exhumation, crustal deformation, and thermal structure of the Nepal Himalaya derived from the inversion of thermochronological and thermobarometric data. J. Geophys. Res. 115, B06407.
Hirschmann, G., Duyster, J., Harms, U., Kontny, A., Lapp, M., de Wall, H., Zulauf, G., 1997. The KTB superdeep borehole: petrography and structure of a 9-km-deep crustal section. Geol. Rundsch. 86, 3–14.
Huntley, D.J., Lamothe, M., 2001. Ubiquity of anomalous fading in K-feldspars and the measurement and correction for it in optical dating. Can. J. Earth Sci. 38 (7), 1093–1106.
Huntley, D.J., 2006. An explanation of the power-law decay of luminescence. J. Phys. Condens. Matter 18, 1359–1365.
Kars, R.H., Wallinga, J., Cohen, K.M., 2008. A new approach towards anomalous fading correction for feldspar IRSL dating —tests on samples in field saturation. Radiat. Meas. 43 (2–6), 786–790.
King, G.E., Herman, F., Lambert, R., Valla, P.G., Guralnik, B., 2016a. Multi-OSL thermochronometry of feldspar. Quat. Geochronol. 33, 76–87.
King, G.E., Herman, F., Guralnik, B., 2016b. Northward migration of the eastern Himalayan syntaxis revealed by OSL thermochronometry. Science 353 (6301), 800–804.
King, G.E., Tsukamoto, S., Herman, F., Biswas, R.H., Sueoka, S., Tagami, T., 2020. Electron spin resonance (ESR) thermochronometry of the Hida range of the Japanese Alps: validation and future potential. Geochronology 2, 1–15.
Kook, M.H., Lapp, T., Murray, A.S., Thiel, C., 2012. A Risø XRF Attachment for Major Element Analysis of Aliquots of Quartz and Feldspar Separates. UK Luminescence and ESR Meeting, Aberystwyth, p. 37. September 2012 (abstract).
Lambert, R., 2018. Investigating Thermal Decay in K-Feldspar for the Application of IRSL Thermochronometry on the Mont Blanc Massif. PhD thesis. University of Lausanne, 139.
Li, B., Li, S.-H., 2008. Investigations of the dose-dependent anomalous fading rate of feldspar from sediments. J. Phys. D Appl. Phys. 41, 15, 225502.
Li, B., Li, S.-H., 2011. Luminescence dating of K-feldspar from sediments: a protocol without anomalous fading correction. Quat. Geochronol. 6 (5), 468–479.
Li, B., Li, S.-H., 2012. Determining the cooling age using luminescence-thermochronology. Tectonophysics 580, 242–248.
Li, B., Li, S.-H., 2013. The effect of band-tail states on the thermal stability of the infrared stimulated luminescence from K-feldspar. J. Lumin. 136, 5–10.
Murray, A.S., Wintle, A.G., 1999. Isothermal decay of optically stimulated luminescence in quartz. Radiat. Meas. 30, 119–125.
Poolton, N.R.J., Kars, R.H., Wallinga, J., Bos, A.J.J., 2009. Direct evidence for the participation of band-tails and excited-state tunneling in the luminescence of irradiated feldspars. J. Phys. Condens. Matter 21, 1–10.
Rhodes, E.J., 2011. Optically stimulated luminescence dating of sediments over the past 200.000 years. Annu. Rev. Earth Planet Sci. 39, 461–488.
Riedesel, S., King, G.E., Prasad, A.K., Kumar, R., Finch, A.A., Jain, M., 2019. Optical determination of the width of the band-tail states, and the excited and ground state energies of the principal dosimetric trap in feldspar. Radiat. Meas. 125, 40–51.
Riedesel, S., Bell, A.M.T., Duller, G.A.T., Finch, A.A., Jain, M., King, G.E., Pearce, N.J., Roberts, H.M., 2021. Exploring sources of variation in thermoluminescence emissions and anomalous fading in alkali feldspars. Radiat. Meas. 142, 106541.
Szulc, A.G., Najman, Y., Sinclair, H.D., Pringle, M., Bickle, M., Chapman, H., Garzanti, E., Andò, S., Huyghe, P., Mugnier, J.-L., Ojha, T., DeCelles, P., 2006. Tectonic evolution of the Himalaya constrained by detrital ^{40}Ar-^{39}Ar, Sm-Nd and petrographic data from the Siwalik foreland basin succession, SW Nepal. Basin Res. 18, 375–391.
Tachiya, M., Mozumder, A., 1974. Decay of trapped electrons by tunneling to scavenger molecules in low-temperature glasses. Chem. Phys. Lett. 28 (1), 87–89.
Tarantola, A., 2005. Inverse Problem Theory and Methods for Model Parameter Estimation. Society for Industrial and Applied Mathematics, 342.
Tokuoka, T., Takeda, S., Yoshida, M., Upreti, B.N., 1988. The Churia (Siwalik) Group in the Western Part of the Arung Khola Area, vol. 22. Memoir of the Faculty of Science, Shimane University, West Central Nepal, pp. 131–140.
Wagner, G.A., Coyle, D.A., Duyster, J., Henjes-Kunst, F., Peterek, A., Schröder, B., Stöckhert, B., Wemmer, K., Zulauf, G., Ahrendt, H., Bischoff, R., Hejl, E., Jacobs, J., Menzel, D., Lal, N., Van den Haute, P., Vercoutere, C., Welzel, B., 1997. Post-Variscan thermal and tectonic evolution of the KTB site and its surroundings. J. Geophys. Res. Solid Earth 102 (B8), 18221–18232.
Wallinga, J., Murray, A.S., Wintle, A.G., Bøtter-Jensen, L., 2002. Electron-trapping probability in natural dosemeters as a function of irradiation temperature. Radiat. Protect. Dosim. 101 (1–4), 339–344.

Warnock, A.C., Zeitler, P.K., 1998. $^{40}Ar/^{39}Ar$ thermochronometry of K-feldspar from the KTB borehole, Germany. Earth Planet Sci. Lett. 158, 67–79.
Wheelock, B., Constable, S., Key, K., 2015. The advantages of logarithmically scaled data for electromagnetic inversion. Geophys. J. Int. 201, 1765–1780.
Wintle, A.G., 1973. Anomalous fading of thermoluminescence in mineral samples. Nature 245, 143–144.
Wintle, A.G., 1977. Detailed study of a thermoluminescent mineral exhibiting anomalous fading. J. Lumin. 15, 385–393.
Wu, T.-S., Jain, M., Guralnik, B., Murray, A.S., Chen, Y.-G., 2015. Luminescence characteristics of quartz from Hsuehshan range (central Taiwan) and implications for thermochronometry. Radiat. Meas. 81, 104–109.